Determination of the atmospheric neutrino flux and searches for new physics with AMANDA-II

R. Abbasi,[23] Y. Abdou,[17] M. Ackermann,[35] J. Adams,[13] M. Ahlers,[27] K. Andeen,[23] J. Auffenberg,[34] X. Bai,[26] M. Baker,[23] S. W. Barwick,[19] R. Bay,[7] J. L. Bazo Alba,[35] K. Beattie,[8] S. Bechet,[10] J. K. Becker,[16] K.-H. Becker,[34] M. L. Benabderrahmane,[35] J. Berdermann,[35] P. Berghaus,[23] D. Berley,[14] E. Bernardini,[35] D. Bertrand,[10] D. Z. Besson,[21] M. Bissok,[1] E. Blaufuss,[14] D. J. Boersma,[23] C. Bohm,[29] J. Bolmont,[35] S. Böser,[35] O. Botner,[32] L. Bradley,[31] J. Braun,[23] D. Breder,[34] T. Burgess,[29] T. Castermans,[25] D. Chirkin,[23] B. Christy,[14] J. Clem,[26] S. Cohen,[20] D. F. Cowen,[31,30] M. V. D'Agostino,[7] M. Danninger,[13] C. T. Day,[8] C. De Clercq,[11] L. Demirörs,[20] O. Depaepe,[11] F. Descamps,[17] P. Desiati,[23] G. de Vries-Uiterweerd,[17] T. DeYoung,[31] J. C. Diaz-Velez,[23] J. Dreyer,[16] J. P. Dumm,[23] M. R. Duvoort,[33] W. R. Edwards,[8] R. Ehrlich,[14] J. Eisch,[23] R. W. Ellsworth,[14] O. Engdegård,[32] S. Euler,[1] P. A. Evenson,[26] O. Fadiran,[4] A. R. Fazely,[6] T. Feusels,[17] K. Filimonov,[7] C. Finley,[23] M. M. Foerster,[31] B. D. Fox,[31] A. Franckowiak,[9] R. Franke,[35] T. K. Gaisser,[26] J. Gallagher,[22] R. Ganugapati,[23] L. Gerhardt,[8,7] L. Gladstone,[23] A. Goldschmidt,[8] J. A. Goodman,[14] R. Gozzini,[24] D. Grant,[31] T. Griesel,[24] A. Groß,[13,18] S. Grullon,[23] R. M. Gunasingha,[6] M. Gurtner,[34] C. Ha,[31] A. Hallgren,[32] F. Halzen,[23] K. Han,[13] K. Hanson,[23] Y. Hasegawa,[12] J. Heise,[33] K. Helbing,[34] P. Herquet,[25] S. Hickford,[13] G. C. Hill,[23] K. D. Hoffman,[14] K. Hoshina,[23] D. Hubert,[11] W. Huelsnitz,[14] J.-P. Hülß,[1] P. O. Hulth,[29] K. Hultqvist,[29] S. Hussain,[26] R. L. Imlay,[6] M. Inaba,[12] A. Ishihara,[12] J. Jacobsen,[23] G. S. Japaridze,[4] H. Johansson,[29] J. M. Joseph,[8] K.-H. Kampert,[34] A. Kappes,[23,*] T. Karg,[34] A. Karle,[23] J. L. Kelley,[23,†] P. Kenny,[21] J. Kiryluk,[8,7] F. Kislat,[35] S. R. Klein,[8,7] S. Klepser,[35] S. Knops,[1] G. Kohnen,[25] H. Kolanoski,[9] L. Köpke,[24] M. Kowalski,[9] T. Kowarik,[24] M. Krasberg,[23] K. Kuehn,[15] T. Kuwabara,[26] M. Labare,[10] K. Laihem,[1] H. Landsman,[23] R. Lauer,[35] H. Leich,[35] D. Lennarz,[1] A. Lucke,[9] J. Lundberg,[32] J. Lünemann,[24] J. Madsen,[28] P. Majumdar,[35] R. Maruyama,[23] K. Mase,[12] H. S. Matis,[8] C. P. McParland,[8] K. Meagher,[14] M. Merck,[23] P. Mészáros,[30,31] E. Middell,[35] N. Milke,[16] H. Miyamoto,[12] A. Mohr,[9] T. Montaruli,[23,‡] R. Morse,[23] S. M. Movit,[30] K. Münich,[16] R. Nahnhauer,[35] J. W. Nam,[19] P. Nießen,[26] D. R. Nygren,[8,29] S. Odrowski,[18] A. Olivas,[14] M. Olivo,[32] M. Ono,[12] S. Panknin,[9] S. Patton,[8] C. Pérez de los Heros,[32] J. Petrovic,[10] A. Piegsa,[24] D. Pieloth,[35] A. C. Pohl,[32,§] R. Porrata,[7] N. Potthoff,[34] P. B. Price,[7] M. Prikockis,[31] G. T. Przybylski,[8] K. Rawlins,[3] P. Redl,[14] E. Resconi,[18] W. Rhode,[16] M. Ribordy,[20] A. Rizzo,[11] J. P. Rodrigues,[23] P. Roth,[14] F. Rothmaier,[24] C. Rott,[15] C. Roucelle,[18] D. Rutledge,[31] D. Ryckbosch,[17] H.-G. Sander,[24] S. Sarkar,[27] K. Satalecka,[35] S. Schlenstedt,[35] T. Schmidt,[14] D. Schneider,[23] A. Schukraft,[1] O. Schulz,[18] M. Schunck,[1] D. Seckel,[26] B. Semburg,[34] S. H. Seo,[29] Y. Sestayo,[18] S. Seunarine,[13] A. Silvestri,[19] A. Slipak,[31] G. M. Spiczak,[28] C. Spiering,[35] T. Stanev,[26] G. Stephens,[31] T. Stezelberger,[8] R. G. Stokstad,[8] M. C. Stoufer,[8] S. Stoyanov,[26] E. A. Strahler,[23] T. Straszheim,[14] K.-H. Sulanke,[35] G. W. Sullivan,[14] Q. Swillens,[10] I. Taboada,[5] O. Tarasova,[35] A. Tepe,[34] S. Ter-Antonyan,[6] C. Terranova,[20] S. Tilav,[26] M. Tluczykont,[35] P. A. Toale,[31] D. Tosi,[35] D. Turčan,[14] N. van Eijndhoven,[33] J. Vandenbroucke,[7] A. Van Overloop,[17] B. Voigt,[35] C. Walck,[29] T. Waldenmaier,[9] M. Walter,[35] C. Wendt,[23] S. Westerhoff,[23] N. Whitehorn,[23] C. H. Wiebusch,[1] A. Wiedemann,[16] G. Wikström,[29] D. R. Williams,[2] R. Wischnewski,[35] H. Wissing,[1,14] K. Woschnagg,[7] X. W. Xu,[6] G. Yodh,[19] and S. Yoshida[12]

(IceCube Collaboration)[‖]

[1]*III Physikalisches Institut, RWTH Aachen University, D-52056 Aachen, Germany*
[2]*Department of Physics and Astronomy, University of Alabama, Tuscaloosa, Alabama 35487, USA*
[3]*Department of Physics and Astronomy, University of Alaska Anchorage, 3211 Providence Dr., Anchorage, Alaska 99508, USA*
[4]*CTSPS, Clark-Atlanta University, Atlanta, Georgia 30314, USA*
[5]*School of Physics and Center for Relativistic Astrophysics, Georgia Institute of Technology, Atlanta, Georgia 30332, USA*
[6]*Department of Physics, Southern University, Baton Rouge, Louisiana 70813, USA*
[7]*Department of Physics, University of California, Berkeley, California 94720, USA*
[8]*Lawrence Berkeley National Laboratory, Berkeley, California 94720, USA*
[9]*Institut für Physik, Humboldt-Universität zu Berlin, D-12489 Berlin, Germany*
[10]*Université Libre de Bruxelles, Science Faculty CP230, B-1050 Brussels, Belgium*
[11]*Vrije Universiteit Brussel, Dienst ELEM, B-1050 Brussels, Belgium*
[12]*Department of Physics, Chiba University, Chiba 263-8522, Japan*
[13]*Department of Physics and Astronomy, University of Canterbury, Private Bag 4800, Christchurch, New Zealand*
[14]*Department of Physics, University of Maryland, College Park, Maryland 20742, USA*
[15]*Department of Physics and Center for Cosmology and Astro-Particle Physics, Ohio State University, 191 W. Woodruff Avenue, Columbus, Ohio 43210, USA*
[16]*Department of Physics, TU Dortmund University, D-44221 Dortmund, Germany*

 © 2009 The American Physical Society

[17]*Department of Subatomic and Radiation Physics, University of Gent, B-9000 Gent, Belgium*
[18]*Max-Planck-Institut für Kernphysik, D-69177 Heidelberg, Germany*
[19]*Department of Physics and Astronomy, University of California, Irvine, California 92697, USA*
[20]*Laboratory for High Energy Physics, École Polytechnique Fédérale, CH-1015 Lausanne, Switzerland*
[21]*Department of Physics and Astronomy, University of Kansas, Lawrence, Kansas 66045, USA*
[22]*Department of Astronomy, University of Wisconsin, Madison, Wisconsin 53706, USA*
[23]*Department of Physics, University of Wisconsin, Madison, Wisconsin 53706, USA*
[24]*Institute of Physics, University of Mainz, Staudinger Weg 7, D-55099 Mainz, Germany*
[25]*University of Mons-Hainaut, 7000 Mons, Belgium*
[26]*Bartol Research Institute and Department of Physics and Astronomy, University of Delaware, Newark, Delaware 19716, USA*
[27]*Department of Physics, University of Oxford, 1 Keble Road, Oxford OX1 3NP, UK*
[28]*Department of Physics, University of Wisconsin, River Falls, Wisconsin 54022, USA*
[29]*Department of Physics, Stockholm University, SE-10691 Stockholm, Sweden*
[30]*Department of Astronomy and Astrophysics, Pennsylvania State University, University Park, Pennsylvania 16802, USA*
[31]*Department of Physics, Pennsylvania State University, University Park, Pennsylvania 16802, USA*
[32]*Department of Physics and Astronomy, Uppsala University, Box 516, S-75120 Uppsala, Sweden*
[33]*Department of Physics and Astronomy, Utrecht University/SRON, NL-3584 CC Utrecht, The Netherlands*
[34]*Department of Physics, University of Wuppertal, D-42119 Wuppertal, Germany*
[35]*DESY, D-15735 Zeuthen, Germany*

(Received 5 February 2009; published 29 May 2009)

The AMANDA-II detector, operating since 2000 in the deep ice at the geographic South Pole, has accumulated a large sample of atmospheric muon neutrinos in the 100 GeV to 10 TeV energy range. The zenith angle and energy distribution of these events can be used to search for various phenomenological signatures of quantum gravity in the neutrino sector, such as violation of Lorentz invariance or quantum decoherence. Analyzing a set of 5511 candidate neutrino events collected during 1387 days of livetime from 2000 to 2006, we find no evidence for such effects and set upper limits on violation of Lorentz invariance and quantum decoherence parameters using a maximum likelihood method. Given the absence of evidence for new flavor-changing physics, we use the same methodology to determine the conventional atmospheric muon neutrino flux above 100 GeV.

DOI: 10.1103/PhysRevD.79.102005 PACS numbers: 95.55.Vj, 03.65.Yz, 11.30.Cp, 14.60.St

I. INTRODUCTION

Experimental searches for possible low-energy signatures of quantum gravity (QG) can provide a valuable connection to a Planck-scale theory. Numerous quantum gravity theories suggest that Lorentz invariance may be violated or spontaneously broken, including loop quantum gravity [1], noncommutative geometry [2], and string theory [3]. This, in turn, has encouraged phenomenological developments and experimental searches for such effects [4,5]. Space-time may also exhibit a ''foamy'' nature at the smallest length scales, inducing decoherence of pure quantum states to mixed states during propagation through this background [6].

The neutrino sector is a promising place to search for such phenomena. Neutrino oscillations act as a quantum interferometer, and QG effects that are expected to be small at energies below the Planck scale can be amplified into large flavor-changing signatures. Water-based or ice-based Cherenkov neutrino detectors such as BAIKAL [7], AMANDA-II [8], ANTARES [9], and IceCube [10] have the potential to accumulate large samples of high energy atmospheric muon neutrinos. We present here an analysis of AMANDA-II atmospheric muon neutrinos collected from 2000 to 2006 in which we search for flavor-changing signatures that might arise from QG phenomena.

In addition to searches for physics beyond the standard model, a measurement of the conventional atmospheric neutrino flux is useful in its own right. Uncertainties in the incident primary cosmic ray spectrum and in the high energy hadronic interactions affect the atmospheric neutrino flux calculations (see e.g. Refs. [11,12]). Atmospheric neutrinos are the primary background to searches for astrophysical neutrino point sources and diffuse fluxes, so knowledge of the flux at higher energies is crucial. In this analysis, we vary the normalization and spectral index of existing models for the atmospheric neutrino flux and determine the best-fit spectrum.

We begin with a review of the phenomenology relevant to our search for new physics in atmospheric neutrinos. Next, we describe the AMANDA-II detector, data selection

*On leave of absence from Universität Erlangen-Nürnberg, Physikalisches Institut, D-91058, Erlangen, Germany.
†Corresponding author.
jkelley@icecube.wisc.edu
‡On leave of absence from Università di Bari and Sezione INFN, Dipartimento di Fisica, I-70126, Bari, Italy.
§Affiliated with School of Pure and Applied Natural Sciences, Kalmar University, S-39182 Kalmar, Sweden.
‖http://www.icecube.wisc.edu

procedures, and atmospheric neutrino simulation. Third, we describe the analysis methodology by which we quantify any deviation from conventional physics. We do not observe any such deviation, and hence we present upper limits on violation of Lorentz invariance (VLI) and quantum decoherence (QD) obtained with this methodology, as well as a determination of the conventional atmospheric neutrino flux.

II. PHENOMENOLOGY

A. Atmospheric neutrinos

Atmospheric neutrinos are produced when high energy cosmic rays collide with air molecules, producing charged pions and kaons that subsequently decay into muons and muon neutrinos. Observations of atmospheric neutrinos by Super-Kamiokande [13], Soudan 2 [14], MACRO [15], and other experiments have provided strong evidence for mass-induced atmospheric neutrino oscillations. The relationship between the mass eigenstates and the flavor eigenstates can be characterized by three mixing angles, two mass splittings, and a complex phase. Because of the smallness of the θ_{13} mixing angle and the Δm_{12} splitting (see Ref. [16] for a review), it suffices to consider a two-neutrino system in the atmospheric case, and the survival probability for muon neutrinos of energy E as they travel over a baseline L from the production point in the atmosphere to a detector is

$$P_{\nu_\mu\to\nu_\mu} = 1 - \sin^2 2\theta_{\rm atm}\sin^2\left(\frac{\Delta m^2_{\rm atm}L}{4E}\right), \qquad (1)$$

where L is in inverse energy units (we continue this convention unless noted otherwise). In practice, the zenith angle of the neutrino serves as a proxy for the baseline L.

A recent global fit to oscillation data results in best-fit atmospheric oscillation parameters of $\Delta m^2_{\rm atm} = 2.39 \times 10^{-3}$ eV^2 and $\sin^2 2\theta_{\rm atm} = 0.995$ [16]. Thus, for energies above about 50 GeV, atmospheric neutrino oscillations cease for Earth-diameter baselines. However, a number of phenomenological models of physics beyond the standard model predict flavor-changing effects at higher energies that can alter the zenith angle distribution and energy spectrum of atmospheric muon neutrinos. We review two of these here, violation of Lorentz invariance and quantum decoherence.

B. Violation of Lorentz invariance

Many models of quantum gravity suggest that Lorentz symmetry may not be exact [5]. Even if a QG theory is Lorentz symmetric, the symmetry may still be spontaneously broken in our Universe. Atmospheric neutrinos, with energies above 100 GeV and mass less than 1 eV, have Lorentz boosts exceeding 10^{11} and provide a sensitive test of Lorentz symmetry.

Neutrino oscillations, in particular, provide a sensitive test bed for such effects. Oscillations act as a ''quantum interferometer'' by magnifying small differences in energy into large flavor changes as the neutrinos propagate. In conventional oscillations, this energy shift results from the small differences in mass among the eigenstates, but specific manifestations of VLI can also result in energy shifts that can generate neutrino oscillations with different energy dependencies.

In particular, we consider VLI in which neutrinos have limiting velocities other than the canonical speed of light c ([17,18]; see the appendix for further background). Since these velocity eigenstates can be distinct from the mass or flavor eigenstates, in a two-flavor system this introduces another mixing angle ξ and a phase η. The magnitude of the VLI is characterized by the velocity-splitting between the eigenstates, $\Delta c/c = (c_{a1} - c_{a2})/c$.

In this form of VLI, the ν_μ survival probability is [19]

$$P_{\nu_\mu\to\nu_\mu} = 1 - \sin^2 2\Theta\sin^2\left(\frac{\Delta m^2 L}{4E}\mathcal{R}\right), \qquad (2)$$

where the combined effective mixing angle Θ can be written

$$\sin^2 2\Theta = \frac{1}{\mathcal{R}^2}(\sin^2 2\theta + R^2\sin^2 2\xi + 2R\sin 2\theta\sin 2\xi\cos\eta), \qquad (3)$$

the correction to the oscillation wavelength $\mathcal{R}$ is

$$\mathcal{R} = \sqrt{1 + R^2 + 2R(\cos 2\theta\cos 2\xi + \sin 2\theta\sin 2\xi\cos\eta)}, \qquad (4)$$

and the ratio R between the VLI oscillation wavelength and mass-induced wavelength is

$$R = \frac{\Delta c}{c}\frac{E}{2}\frac{4E}{\Delta m^2} \qquad (5)$$

for a muon neutrino of energy E and traveling over baseline L. For atmospheric neutrinos, we fix the conventional mixing angle $\theta = \theta_{\rm atm}$ and mass difference $\Delta m^2 = \Delta m^2_{\rm atm}$ to the global fit values determined in Ref. [20] of $\Delta m^2_{\rm atm} = 2.2 \times 10^{-3}$ eV^2 and $\sin^2 2\theta_{\rm atm} = 1$. For simplicity, the phase η is often set to 0 or $\pi/2$. For illustration, if we take both conventional and VLI mixing to be maximal ($\xi = \theta = \pi/4$), this reduces to

$$P_{\nu_\mu\to\nu_\mu}(\text{maximal}) = 1 - \sin^2\left(\frac{\Delta m^2 L}{4E} + \frac{\Delta c}{c}\frac{LE}{2}\right). \qquad (6)$$

Note the different energy dependence of the two effects. The survival probability for maximal baselines as a function of neutrino energy is shown in Fig. 1.

Several neutrino experiments have set upper limits on this manifestation of VLI, including MACRO [21], Super-Kamiokande [22], and a combined analysis of K2K [23] and Super-Kamiokande data [19] ($\Delta c/c < 2.0 \times 10^{-27}$ at

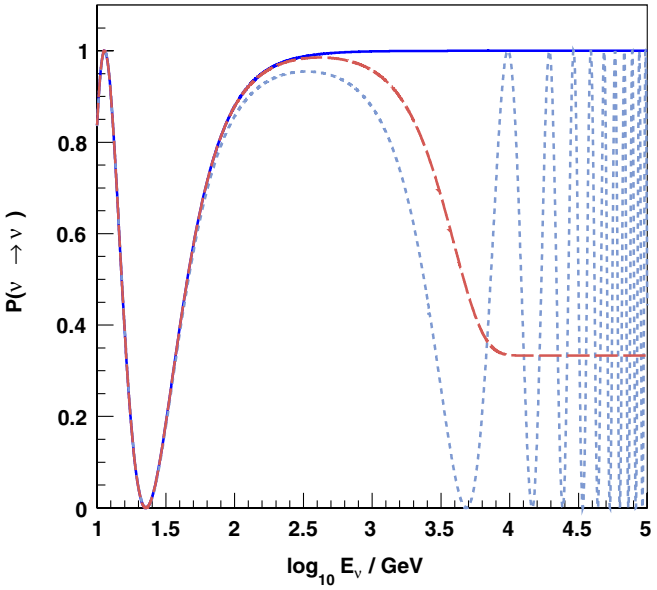


FIG. 1 (color online). ν_μ survival probability as a function of neutrino energy for maximal baselines ($L \approx 2R_{\mathrm{Earth}}$) given conventional oscillations (solid line), VLI (dotted line, with $n = 1$, $\sin 2\xi = 1$, and $\Delta\delta = 10^{-26}$), and QD effects (dashed line, with $n = 2$ and $D^* = 10^{-30}$ GeV^{-1}).

the 90% confidence level (CL) for maximal mixing). In previous work, AMANDA-II has set a preliminary upper limit using four years of data of 5.3×10^{-27} [24]. Other neutrino telescopes, such as ANTARES, are also expected to be sensitive to such effects (see e.g. Ref. [25]).

Given the specificity of this particular model of VLI, we wish to generalize the oscillation probability in Eq. (2). We follow the approach in [25], which is to generalize the VLI oscillation length $L \propto E^{-1}$ to other integral powers of the neutrino energy E, that is,

$$\frac{\Delta c}{c}\frac{LE}{2} \to \Delta\delta\frac{LE^n}{2}, \tag{7}$$

where $n \in \{1, 2, 3\}$, and the generalized VLI term $\Delta\delta$ is in units of GeV^{-n+1}. An $L \propto E^{-2}$ energy dependence ($n = 2$) has been proposed in the context of loop quantum gravity [26] and in the case of nonrenormalizable VLI effects caused by the space-time foam [27]. Both the $L \propto E^{-1}$ ($n = 1$) and the $L \propto E^{-3}$ ($n = 3$) cases have been examined in the context of violations of the equivalence principle [28–30]. In general, Lorentz violation implies violation of the equivalence principle, so searches for either effect are related [5].

C. Quantum decoherence

Another possible low-energy signature of QG is the evolution of pure states to mixed states via interaction with the environment of space-time itself, or quantum decoherence. One heuristic picture of this phenomenon is the production of virtual black hole pairs in a foamy space-time, created from the vacuum at scales near the Planck length [31]. Interactions with the virtual black holes may not preserve certain quantum numbers like neutrino flavor, causing decoherence into a superposition of flavors.

Quantum decoherence can be treated phenomenologically as a quantum open system that evolves thermodynamically (we refer the reader to the appendix for more detail). In a three-flavor neutrino system, the decoherence from one flavor state to a superposition of flavors can be characterized by a set of parameters D_i, $i \in \{1, \ldots, 8\}$ that represent a characteristic inverse length scale over which the decoherence sets in. The ν_μ survival probability in such a system is [32]

$$P_{\nu_\mu\to\nu_\mu} = \frac{1}{3} + \frac{1}{2}\left[\frac{1}{4}e^{-LD_3}(1 + \cos 2\theta)^2 + \frac{1}{12}e^{-LD_8}(1 - 3\cos 2\theta)^2 + e^{-(L/2)(D_6+D_7)}\sin^2 2\theta \cdot \left(\cos\left[\frac{L}{2}\sqrt{\left(\frac{\Delta m^2}{E}\right)^2 - (D_6 - D_7)^2}\right] + \frac{\sin[\frac{L}{2}\sqrt{(\frac{\Delta m^2}{E})^2 - (D_6 - D_7)^2}](D_6 - D_7)}{\sqrt{(\frac{\Delta m^2}{E})^2 - (D_6 - D_7)^2}}\right)\right]. \tag{8}$$

Note the limiting probability of 1/3, representing full decoherence into an equal superposition of flavors. The D_i not appearing in Eq. (8) affect decoherence between other flavors, but not the ν_μ survival probability.

The energy dependence of the decoherence terms D_i depends on the underlying microscopic model. As with the VLI effects, we choose a generalized phenomenological approach where we suppose the D_i vary as some integral power of the energy, that is

$$D_i = D_i^* E^n, \qquad n \in \{1, 2, 3\}, \tag{9}$$

where E is the neutrino energy in GeV, and the units of the D_i^* are GeV^{-n+1}. The particularly interesting E^2 form is suggested by decoherence calculations in noncritical string theories involving recoiling D-brane geometries [33]. We show the $n = 2$ survival probability as a function of neutrino energy for maximal baselines in Fig. 1.

An analysis of Super-Kamiokande in a two-flavor framework has resulted in an upper limit at the 90% CL of $D^* < 9.0 \times 10^{-28}$ GeV^{-1} for an E^2 model and all D_i^* equal [34]. ANTARES has reported sensitivity to various two-flavor decoherence scenarios as well, using a more general formulation [35]. Analyses of Super-Kamiokande, KamLAND, and K2K data [36,37] have also set strong

limits on decoherence effects proportional to E^0 and E^{-1}. Because for such effects our higher energy range does not benefit us, we do not expect to be able to improve upon these limits, and we focus on effects with $n \geq 1$.

III. DATA AND SIMULATION

A. The AMANDA-II detector

The AMANDA-II detector consists of 677 optical modules (OMs) on 19 vertical cables or ''strings'' frozen into the deep, clear ice near the geographic South Pole. Each OM consists of a 20 cm diameter photomultiplier tube housed in a glass pressure sphere. Cherenkov photons produced by charged particles moving through the ice trigger the photomultiplier tubes. Combining the photon arrival times with knowledge of the absorption and scattering properties of the ice [38] allows reconstruction of a particle track through the array [39].

In particular, a charged current ν_μ interaction will produce a muon that can traverse the entire detector. This tracklike topology allows reconstruction of the original neutrino direction to within a few degrees. An estimate of the energy of the muon is possible by measuring its energy loss, but this is complicated by stochastic losses, and in any case is only a lower bound on the original neutrino energy.

B. Simulation

In order to meaningfully compare our data with expectations from various signal hypotheses, we must have a detailed simulation of the atmospheric neutrinos and the subsequent detector response. For the input atmospheric muon neutrino spectrum, we generate an isotropic power-law flux with the NUSIM neutrino simulator [40] and then reweight the events to standard flux predictions [11,41]. We have extended the predicted fluxes to the TeV energy range by fitting the low-energy region with the Gaisser parametrization [42] and then extrapolating above 700 GeV. We add standard oscillations and/or nonstandard flavor changes by weighting the events with the muon neutrino survival probability in Eqs. (1), (2), or (8).

Muon propagation and energy loss near and within the detector is simulated using MMC [43]. Photon propagation through the ice, including scattering and absorption, is modeled with PHOTONICS [44], incorporating the depth-dependent characteristic dust layers [38]. The AMASIM program [45] simulates the detector response, and identical reconstruction methods are performed on data and simulation. Cosmic ray background rejection is verified at all but the highest quality levels by a parallel simulation chain fed with atmospheric muons from CORSIKA [46], although when reaching contamination levels of $O(1\%)$—a rejection factor of 10^8—computational limitations become prohibitive.

C. Atmospheric neutrino event selection

Even with kilometers of ice as an overburden, atmospheric muon events dominate over neutrino events by a factor of about 10^6. Selecting only ''up-going'' muons allows us to reject the large background of atmospheric muons, using the Earth as a filter to screen out everything but neutrinos. In practice, we must also use other observables indicating the quality of the muon directional reconstruction, in order to eliminate misreconstructed atmospheric muon events.

Our data sample consists of 1.3×10^{10} events collected with AMANDA-II during the years 2000 to 2006. The primary trigger for this analysis is a multiplicity condition requiring 24 OMs to exceed their discriminator threshold (a ''hit'') within a sliding window of 2.5 μs. As part of the initial data cleaning, periods of unstable detector operation are discarded, such as during the austral summer months when upgrades and configuration changes occur. After accounting for inherent detector dead time in the trigger and readout electronics, the sample represents 1387 days of live time. During the data filtering, dead or unstable OMs are removed, resulting in approximately 540 modules for use in this analysis. Isolated noise hits and hits caused by electrical cross talk are also removed [39].

As a starting point for neutrino selection, we utilize the quality selection criteria from the AMANDA-II 5-yr point source analysis [47]. These cuts, not specifically optimized for high energy neutrinos, are efficient at the selection of atmospheric neutrinos and achieve a purity level of $\sim$95%, estimated by tightening the quality cuts until the ratio between data and atmospheric neutrino simulation stabilizes. The primary reconstruction and/or quality variables used in this selection are

(1) the reconstructed zenith angle as obtained from a 32-iteration *unbiased likelihood* (UL) fit;
(2) the smoothness, a topological parameter describing the homogeneity of the photon hits along the UL fit track;
(3) the estimated angular resolution of the UL fit, using the width of the likelihood minimum [48];
(4) the likelihood ratio between the UL fit and a *Bayesian likelihood* (BL) fit [49], obtained by weighting the likelihood with a zenith-angle-dependent prior. This weight constrains the track hypothesis to reconstruct the event as a ''down-going'' atmospheric muon.

The strength of the smoothness and the likelihood ratio cuts also vary with the reconstructed zenith angle, as in general the cuts must be stronger near the horizon where background contamination is worse. Further discussion of the background rejection of these quality variables can be found in the point source analysis using these data [50].

To this selection we add further criteria to remove the final few percent of misreconstructed atmospheric muons.

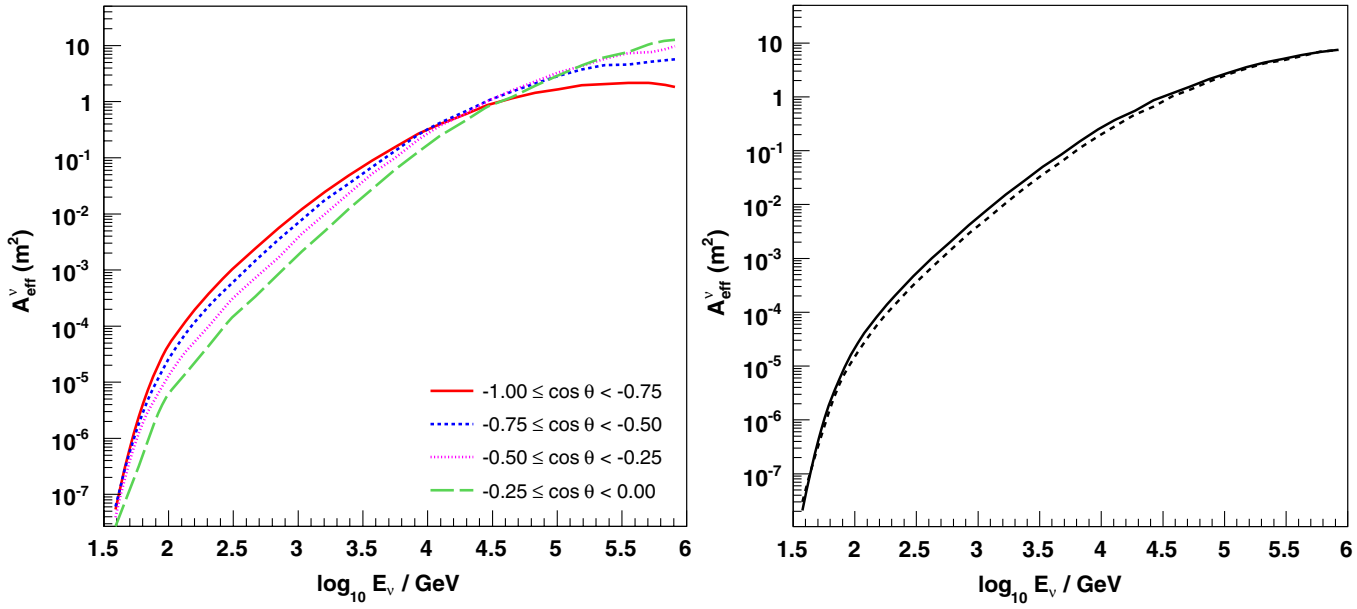


FIG. 2 (color online). Simulated detector effective area versus neutrino energy at the final analysis level. Left: ν_μ effective areas for several zenith angle ranges. Right: zenith-angle-averaged effective areas for ν_μ (solid line) and $\bar{\nu}_\mu$ (dotted line).

Specifically, we remove events with poor values in the following quality variables:

(1) the space-angle difference between the UL fit track and the fit track by JAMS (a fast pattern-matching reconstruction; see Ref. [47]);
(2) the number of hits from direct (unscattered) photons based on the UL fit hypothesis;
(3) the maximum length along the reconstructed track between direct photon hits.

These selection criteria, as well as the analysis procedure described in Sec. IV, were designed in a blind manner, in order to avoid biasing the results. Specifically, our observables (the zenith angle and number of OMs hit, $N_{\rm ch}$; see Sec. IV A) were kept hidden when designing both. However, after unblinding, we found a small excess of high energy events above atmospheric neutrino predictions (444 events with $60 \leq N_{\rm ch} < 120$ on an expectation of $\sim$350). While this is a relatively small fraction of the overall sample, and an excess at high $N_{\rm ch}$ cannot be misinterpreted as one of our new physics hypotheses, a concentration of high energy background events could falsely suggest an atmospheric neutrino spectrum much harder than expected.

We find that these events exhibit characteristics of misreconstructed atmospheric muons: poor reconstructed angular resolution, poor UL-to-BL likelihood ratio, and low numbers of unscattered photon hits based on the fit hypothesis. As atmospheric neutrino events show better angular resolution and likelihood ratio at higher energies, we chose to revise our selection criteria to tighten the cuts on space-angle difference and angular resolution as a function of the number of OMs hit, $N_{\rm ch}$. In particular, from $N_{\rm ch} = 50$ to $N_{\rm ch} = 80$, we linearly decrease (strengthen) the required angular resolution and space-angle difference. These additional cuts were only applied to events with a likelihood ratio less than the median for a given zenith angle, as determined by atmospheric neutrino simulation. We estimate that the purity of the final event sample is greater than 99%.

D. Final neutrino sample

After all selection criteria are applied, we are left with a sample of 5544 atmospheric neutrino candidate events with reconstructed zenith angles below the horizon.[1] We may characterize the total efficiency of neutrino detection, including all detector and cut efficiencies as well as effects such as earth absorption, via the neutrino effective area $A_{\rm eff}^{\nu}(E_\nu, \theta, \phi)$, defined such that

$$N_{\rm events} = \int dE_\nu d\Omega dt \frac{d\Phi(E_\nu, \theta, \phi)}{dE_\nu d\Omega} A_{\rm eff}^{\nu}(E_\nu, \theta, \phi) \quad (10)$$

for a differential neutrino flux $d\Phi/dE_\nu d\Omega$. Figure 2 shows the ν_μ and $\bar{\nu}_\mu$ effective areas as a function of neutrino energy for the event sample used in this analysis, as derived from the simulation chain described in the previous section. We have averaged over the detector azimuth ϕ. The differences in effective area at various zenith angles are due to detector geometry, Earth absorption at high energies, and the strong quality cuts near the horizon; the

[1] A table of the atmospheric neutrino events is available at http://www.icecube.wisc.edu/science/data.

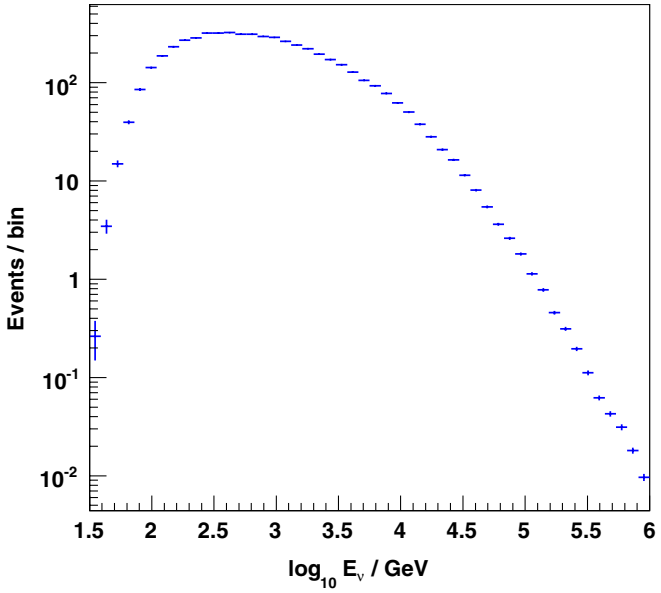


FIG. 3 (color online). Simulated $\nu_\mu + \bar{\nu}_\mu$ energy distribution of the final event sample, assuming the Barr *et al.* input spectrum.

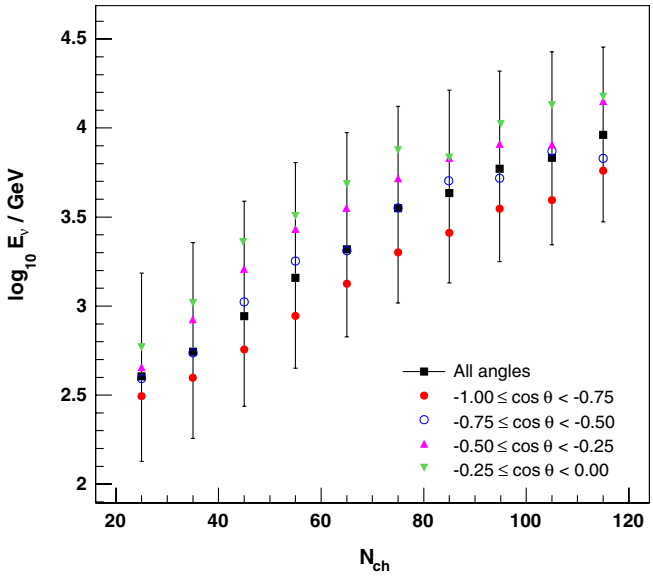


FIG. 4 (color online). Simulated profile histogram of median neutrino energy versus number of OMs hit ($N_{\rm ch}$), both for all zenith angles below the horizon and for various zenith angle ranges. Error bars on the all-angle points represent the $\pm 1\sigma$ spread at each $N_{\rm ch}$.

different effective areas for ν_μ and $\bar{\nu}_\mu$ are due to their different interaction cross sections.

The simulated energy response to the Barr *et al.* atmospheric neutrino flux [41] (without any new physics) is shown in Fig. 3. For this flux, the simulated median energy of the final event sample is 640 GeV, and the 5%–95% range is 105 GeV to 8.9 TeV.

IV. ANALYSIS METHODOLOGY

A. Observables

As described in Sec. II, the signature of a flavor-changing new physics effect such as VLI or QD is a deficit of ν_μ events at the highest energies and longest baselines (i.e., near the vertical direction). For our directional observable, we use the cosine of the reconstructed zenith angle as given by the UL fit, $\cos\theta_{\rm UL}$ (with -1 being the vertical up-going direction). We use the number of OMs (or channels) hit, $N_{\rm ch}$, as an energy-correlated observable. Figure 4 shows the neutrino energy as a function of the simulated $N_{\rm ch}$ response. Figure 5 shows the simulated effects of QD and VLI on both the zenith angle and $N_{\rm ch}$ distributions, a deficit of events at high $N_{\rm ch}$ and toward more vertical directions. Because the $N_{\rm ch}$ energy estimation is approximate, the VLI oscillation minima are smeared out, and the two effects look similar in the observables. Furthermore, the observable minima are not exactly in the vertical direction because the $N_{\rm ch}$-energy relationship varies with the zenith angle (see Fig. 4) since the detector is taller than it is wide. However, this geometry is beneficial for angular reconstruction of near-vertical events and so is still well suited to this analysis.

B. Statistical methods

To test the compatibility of our measured atmospheric neutrino ($\cos\theta_{\rm UL}$, $N_{\rm ch}$) distribution with the various hypotheses characterized by the VLI and QD parameters, we turn to the frequentist approach of Feldman and Cousins [51]. Specifically, we iterate over our physics parameters θ_r, and our test statistic at each point in the parameter space is the log likelihood ratio comparing this to the best-fit point $\hat{\theta}_r$,

$$\begin{aligned}\Delta\mathcal{L}(\theta_r) &= \mathcal{L}(\theta_r) - \mathcal{L}(\hat{\theta}_r) \\ &= -2\ln P(\{n_i\}|\theta_r) + 2\ln P(\{n_i\}|\hat{\theta}_r) \\ &= 2\sum_{i=1}^{N}\left(\mu_i - \hat{\mu}_i + n_i \ln\frac{\hat{\mu}_i}{\mu_i}\right),\end{aligned} \tag{11}$$

for binned distributions of observables with n_i counts in the ith bin, with $\mu_i(\hat{\mu}_i)$ expected given physics parameters $\theta_r(\hat{\theta}_r)$. For example, in a search for VLI effects, our physics parameters θ_r are the VLI parameters $\log_{10}\Delta\delta$ and $\sin 2\xi$; a binned distribution of simulated $N_{\rm ch}$ and $\cos\theta_{\rm UL}$ gives us μ_i for a particular value of the VLI parameters; and the distribution of $N_{\rm ch}$ and $\cos\theta_{\rm UL}$ for the data gives us n_i.

As in Ref. [51], we characterize the spread in the test statistic $\Delta\mathcal{L}$ expected from statistical variations by generating a number of simulated experiments at each point θ_r. To define the allowed region of parameter space at a CL α, we find the critical value $\Delta\mathcal{L}_{\rm crit}(\theta_r)$ for which a fraction α of the experiments at θ_r satisfy $\Delta\mathcal{L} < \Delta\mathcal{L}_{\rm crit}$. Then our

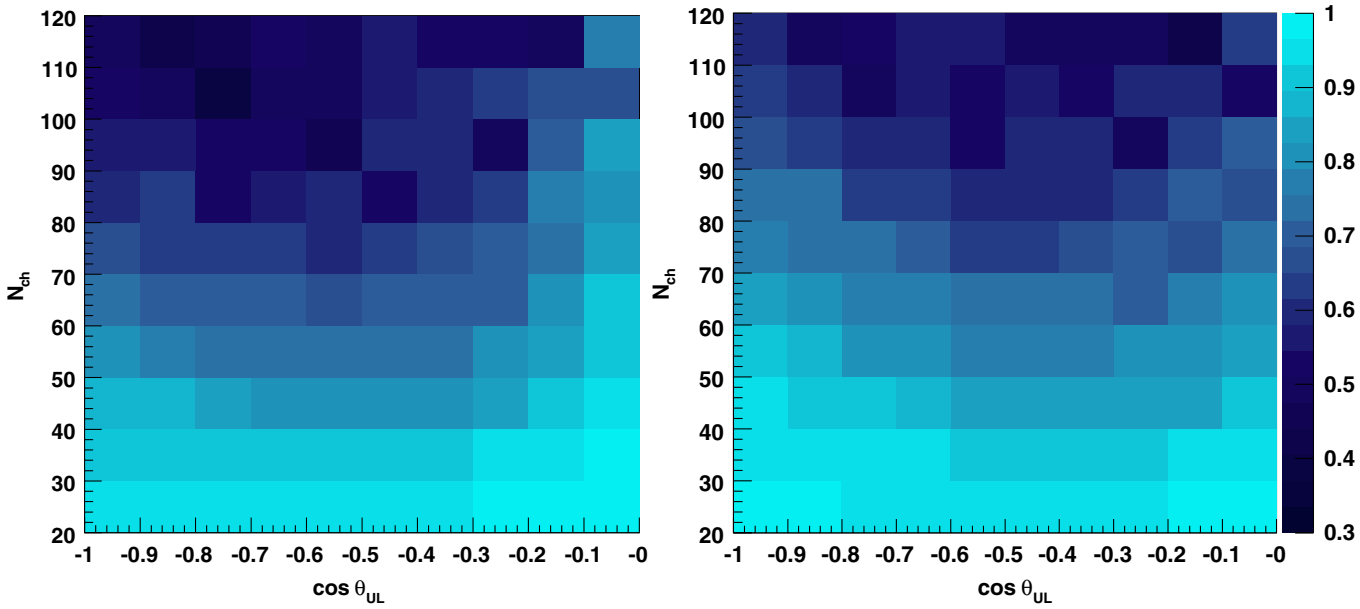


FIG. 5 (color online). Ratio of the simulated number of events given VLI (left, with $n = 1$, $\sin 2\xi = 1$, and $\Delta\delta = 10^{-26}$) and QD (right, with $n = 2$ and $D^* = 10^{-30}$ GeV^{-1}) to conventional oscillation predictions for the zenith angle and N_{ch} distribution.

acceptance region at this CL is the set of parameter space $\{\theta_r\}$ where $\Delta\mathcal{L}_{\text{data}}(\theta_r) < \Delta\mathcal{L}_{\text{crit}}(\theta_r)$.

The above procedure does not *a priori* incorporate any systematic errors (or in statistical terms, *nuisance parameters*). For a review of recent approaches to this problem, see [52]. We use an approximation for the likelihood ratio that, in a sense, uses the worst-case values for the nuisance parameters θ_s—the values that make the data fit the hypothesis the best at the point θ_r. In other words, we marginalize over θ_s in both the numerator and the denominator of the likelihood ratio:

$$\Delta\mathcal{L}_p(\theta_r) = \mathcal{L}(\theta_r, \hat{\hat{\theta}}_s) - \mathcal{L}(\hat{\theta}_r, \hat{\theta}_s), \tag{12}$$

where we have globally minimized the second term, and we have conditionally minimized the first term, keeping θ_r fixed but varying the nuisance parameters to find $\hat{\hat{\theta}}_s$. This test statistic is known as the *profile likelihood* [53].

The profile likelihood is used in combination with a χ^2 approximation in the MINOS method in MINUIT [54] and is also explored in some detail by Rolke *et al.* [55,56]. To extend our frequentist construction to the profile likelihood, we follow the *profile construction* method [57,58]: we perform simulated experiments as before, but instead of iterating through the entire (θ_r, θ_s) space, at each point in the physics parameter space θ_r we fix θ_s to its best-fit value from the *data*, $\hat{\hat{\theta}}_s$. Then we recalculate the profile likelihood for the experiment as defined in Eq. (12). As before, this gives us a set of likelihood ratios $\{\Delta\mathcal{L}_p\}$ with which we can define the critical value for a confidence level that depends only on θ_r.

C. Systematic errors

Each nuisance parameter added to the likelihood test statistic increases the dimensionality of the space we must search for the minimum; therefore, to add systematic errors we group by their effect on the $(\cos\theta_{\text{UL}}, N_{\text{ch}})$ distribution. We define the following four classes of errors: (1) *normalization* errors, affecting only the total event count; (2) *slope* errors, affecting the energy spectrum of the neutrino events and thus the N_{ch} distribution; (3) *tilt* errors, affecting the $\cos\theta_{\text{UL}}$ distribution; and (4) *OM efficiency* errors, which affect the probability of photon detection and change both the $\cos\theta_{\text{UL}}$ and N_{ch} distribution. These errors are incorporated into the simulation as follows:

(i) Normalization errors are incorporated via a uniform weight $1 \pm \sqrt{(\alpha_1^2 + \alpha_2^2)}$;

(ii) slope errors are incorporated via an energy-dependent event weight $(E/E_{\text{median}})^{\Delta\gamma}$, where E_{median} is the median neutrino energy at the final cut level, 640 GeV;

(iii) tilt errors are incorporated by linearly tilting the $\cos\theta_{\text{UL}}$ distribution via a factor $1 + 2\kappa(\cos\theta_{\text{UL}} + \frac{1}{2})$;

(iv) and OM efficiency errors are incorporated by regenerating atmospheric neutrino simulation while changing the efficiency of all OMs in the detector simulation from the nominal value by a factor $1 + \epsilon$.

We split the normalization error into two components, α_1 and α_2, to facilitate the determination of the conventional atmospheric flux, as we discuss later.

TABLE I. Systematic errors in the atmospheric muon neutrino flux, separated by effect on the observables $\cos\theta_{\rm UL}$ and $N_{\rm ch}$ (see Sec. IV C for details on the parameters).

Error	Class	Magnitude
Atm. $\nu_\mu + \bar{\nu}_\mu$ flux	α_1	$\pm 18\%$
Neutrino interaction	α_2	$\pm 8\%$
Reconstruction bias	α_2	-4%
ν_τ-induced muons	α_2	$+2\%$
Background contamination	α_2	$+1\%$
Charmed meson contribution	α_2	$+1\%$
Timing residual uncertainty	α_2	$\pm 2\%$
Muon energy loss	α_2	$\pm 1\%$
Primary spectral slope (H, He)	$\Delta\gamma$	± 0.03
Charmed meson contribution	$\Delta\gamma$	$+0.05$
Pion/kaon ratio	κ	$+0.01/-0.03$
Charmed meson contribution	κ	-0.03
OM efficiency, ice	ϵ	$\pm 10\%$

Table I summarizes sources of systematic error and the class of each error. The total normalization errors α_1 and α_2 are obtained by adding the individual normalization errors in quadrature, while the tilt κ and slope change $\Delta\gamma$ are added linearly. Asymmetric error totals are conservatively assumed to be symmetric, using whichever deviation from the nominal is largest. Each class of error maps to one dimension in the likelihood space, so, for example, in the VLI case, $\mathcal{L}(\theta_r, \theta_s) = \mathcal{L}(\Delta\delta, \sin 2\xi, \alpha, \Delta\gamma, \kappa, \epsilon)$. During minimization, each nuisance parameter is allowed to vary freely within the range allowed around its nominal value, with each point in the likelihood space giving a specific prediction for the observables, $N_{\rm ch}$ and $\cos\theta_{\rm UL}$. In most cases, the nominal value of a nuisance parameter corresponds to the predictions of the Barr *et al.* flux, with best-known inputs to the detector simulation chain.

One of the largest sources of systematic error is the overall normalization of the atmospheric neutrino flux. While the total $\nu_\mu + \bar{\nu}_\mu$ simulated event rate for recent models [11,41] only differs by $\pm 7\%$, this masks significantly larger differences in the individual ν_μ and $\bar{\nu}_\mu$ rates. We take the latter difference of $\pm 18\%$ to be more representative of the true uncertainties in the models. This is also in line with the total uncertainty in the flux estimated in Ref. [11].

Another large source of error in the event rate arises from uncertainties in our simulation of the neutrino interactions, including the neutrino-nucleon cross section, parton distribution functions, and the neutrino-muon scattering angle. We quantify this by comparing our NUSIM simulation with a sample generated with the ANIS simulator [59]. ANIS uses the CTEQ5 cross sections and parton distribution functions [60], compared to Martin-Roberts-Stirling [61] in NUSIM, and it also accurately simulates the neutrino-muon scattering angle. We find an 8% difference in the normalization for an atmospheric neutrino spectrum.

A third significant source of error is the uncertainty in the efficiency of the optical modules, that is, the probability an OM will detect a Cherenkov photon. This has a large effect on both the overall detector event rate (a decrease of 1% in efficiency results in a decrease of 2.5% in event rate) and the shape of the zenith angle and $N_{\rm ch}$ distributions. We quantify the uncertainty by comparing the trigger rate of down-going muons with simulation predictions given various OM efficiencies, including the uncertainty of hadronic interactions by using CORSIKA air shower simulations with the SIBYLL 2.1 [62], EPOS 1.60 [63], and QGSJET-II-03 [64] interaction models. We find that we can constrain the optical module efficiency to within $+10\%/-7\%$, consistent with the range of uncertainty determined in Ref. [47]. Furthermore, because uncertainties in the ice properties have similar effects on our observables, we model OM efficiency and ice scattering/absorption together as a single source of error of $\pm 10\%$ (in efficiency).

Other smaller sources of error were quantified with dedicated simulation studies or, if directly applicable to this analysis, taken from Ref. [47]. For example, we determine the effect of a large contribution of "prompt" ν_μ from charmed particle decay by simulating the optimistic Naumov recombination quark-parton model (RQPM) flux [65], and find that its effects can be modeled with the normalization, slope, and tilt errors as shown in Table I. Finally, we characterize our uncertainty in our reconstruction quality parameters ("reconstruction bias" in Table I) by investigating how systematic disagreements between data and simulation affect the number of events surviving to the final cut level.

D. Binning and analysis parameters

In general, finer binning provides higher sensitivity with a likelihood analysis, and indeed we find a monotonic increase in sensitivity to VLI effects while increasing the number of bins in $\cos\theta_{\rm UL}$ and $N_{\rm ch}$. However, because the further gains in sensitivity are minimal with binning finer than 10×10, we limit ourselves to this size in order to avoid any systematic artifacts that might show up were we to bin, say, finer than our angular resolution. We also limit the $N_{\rm ch}$ range for the analysis to $20 \leq N_{\rm ch} < 120$. While the multiplicity trigger requires 24 or more OMs in an event, the hit-cleaning algorithms reduce the effective threshold to $N_{\rm ch} \approx 20$. We limit the high energy range to events with $N_{\rm ch} < 120$ in order to avoid regions with poor statistics. This limits the possibility that a few remaining background events concentrated at high energy might bias the analysis, which assumes the data can be modeled by atmospheric neutrino simulation with a small energy-*independent* background contamination. The choice of $N_{\rm ch}$ range reduces the number of candidate neutrino events in the analysis region to 5511. These binning choices were made in a blind manner, using simulation to determine sensitivity to the new physics effects.

TABLE II. Physics parameters and nuisance parameters used in each of the likelihood analyses (VLI, QD, and conventional).

Analysis	Physics parameters	Nuisance parameters
VLI	$\Delta\delta$, sin2ξ	α_1, α_2, $\Delta\gamma$, κ, ϵ
QD	$D^*_{3,8}$, $D^*_{6,7}$	α_1, α_2, $\Delta\gamma$, κ, ϵ
Conv.	α_1, $\Delta\gamma$	α_2, κ, ϵ

We also make a few more simplifications to reduce the dimensionality of the likelihood space. First, the phase η in the VLI survival probability [Eq. (2)] is only relevant if the VLI effects are large enough to overlap in energy with conventional oscillations (i.e., below $\sim$100 GeV). Since our neutrino sample is largely outside this range, we set $\cos\eta = 0$ for this search. This means we can also limit the VLI mixing angle to the range $0 \leq \sin2\xi \leq 1$. Second, in the QD case, we vary the decoherence parameters D_i^* in pairs (D_3^*, D_8^*) and (D_6^*, D_7^*). If we set D_3^* and D_8^* to zero, after decoherence $1/2$ of ν_μ remain; with D_6^* and D_7^* set to zero, $5/6$ remain; and with all D_i^* equal and nonzero, $1/3$ remain after decoherence. These limiting behaviors are relevant when considering sensitivity to different parts of the parameter space.

Finally, in the absence of new physics, we can use the same methodology to determine the conventional atmospheric neutrino flux. In this case, the nuisance parameters α_1 (the uncertainty on the atmospheric neutrino flux normalization) and $\Delta\gamma$ (the change in spectral slope relative to the input model) become our physics parameters. The determination of an input energy spectrum by using a set of model curves with a limited number of parameters is commonly known as *forward-folding* (see e.g. Ref. [66]).

Table II summarizes the likelihood parameters used for the VLI, QD, and conventional analyses.

V. RESULTS

After performing the likelihood analysis on the $(\cos\theta_{\rm UL}, N_{\rm ch})$ distribution, we find no evidence for VLI-induced oscillations or quantum decoherence, and the data are consistent with expectations from atmospheric flux models. The reconstructed zenith angle and $N_{\rm ch}$ distributions compared to standard atmospheric neutrino models are shown in Fig. 6, projected into one dimension from the 10×10 two-dimensional analysis distribution and rebinned. Given the lack of evidence for new physics, we set upper limits on the VLI and QD parameters.

A. Upper limits on violation of Lorentz invariance

The 90% CL upper limits on the VLI parameter $\Delta\delta$ for oscillations of various energy dependencies, with maximal mixing ($\sin2\xi = 1$) and phase $\cos\eta = 0$, are presented in Table III. Allowed regions at 90%, 95%, and 99% confidence levels in the $\Delta\delta - \sin2\xi$ plane for the $n = 1$ hypothesis are shown in Fig. 7. The upper limit at maximal mixing of $\Delta\delta \leq 2.8 \times 10^{-27}$ is competitive with that from a combined Super-Kamiokande and K2K analysis [19].

In the $n = 1$ case, recall that the VLI parameter $\Delta\delta$ corresponds to the splitting in velocity eigenstates $\Delta c/c$. Observations of ultrahigh energy cosmic rays constrain VLI velocity-splitting in other particle sectors, with the upper limit on proton-photon splitting of $(c_p - c)/c < 10^{-23}$ [17]. While we probe a rather specific manifestation of VLI in the neutrino sector, our limits are orders of magnitude better than those obtained with other tests.

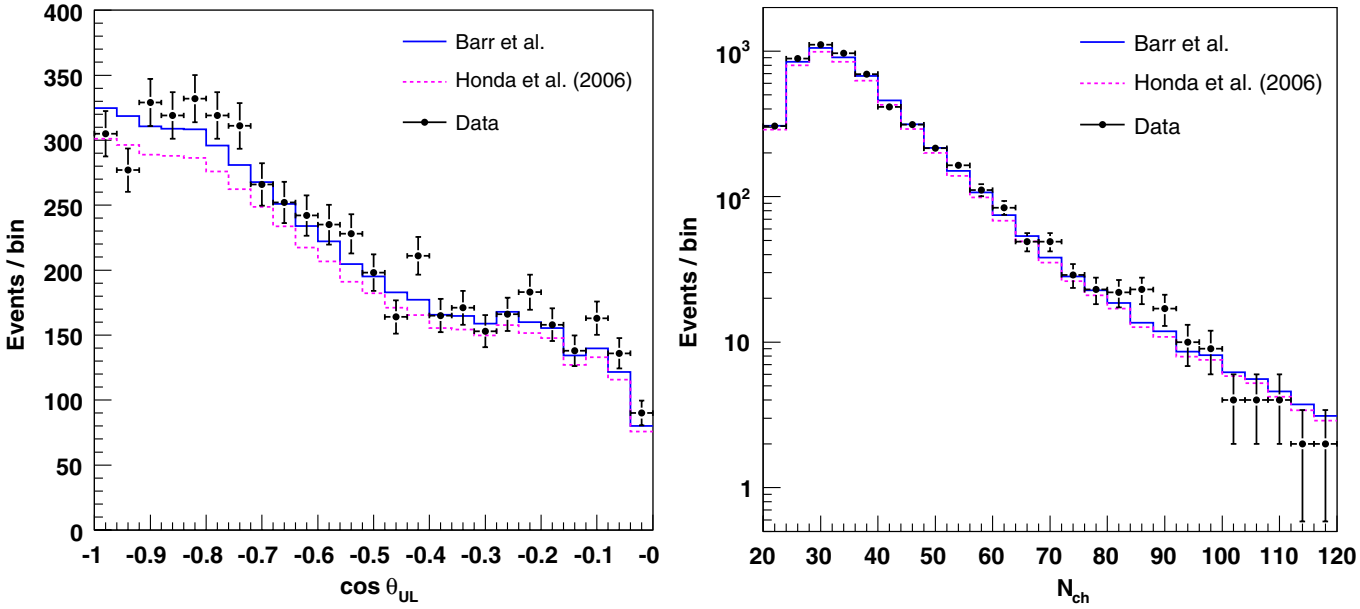


FIG. 6 (color online). Zenith angle and $N_{\rm ch}$ distribution of candidate atmospheric neutrino events in the final sample, compared with Barr *et al.* [41] and Honda *et al.* [11] predictions (statistical error bars).

TABLE III. 90% CL upper limits from this analysis on VLI and QD effects proportional to E^n. VLI upper limits are for the case of maximal mixing ($\sin 2\xi = 1$), and QD upper limits are for the case of $D_3^* = D_8^* = D_6^* = D_7^*$.

n	VLI ($\Delta\delta$)	QD (D^*)	Units
1	2.8×10^{-27}	1.2×10^{-27}	-
2	2.7×10^{-31}	1.3×10^{-31}	GeV^{-1}
3	1.9×10^{-35}	6.3×10^{-36}	GeV^{-2}

B. Upper limits on quantum decoherence

The 90% CL upper limits on the decoherence parameters D_i^* given various energy dependencies are also shown in Table III. Allowed regions at 90%, 95%, and 99% confidence levels in the $D_{3,8}^*$-$D_{6,7}^*$ plane for the $n = 2$ case are shown in Fig. 8. The 90% CL upper limit from this analysis with all D_i^* equal for the $n = 2$ case, $D^* \leq 1.3 \times 10^{-31}\ \mathrm{GeV}^{-1}$, extends the previous best limit from Super-Kamiokande by nearly 4 orders of magnitude. Because of the strong E^2 energy dependence, AMANDA-II's extended energy reach allows much improved limits.

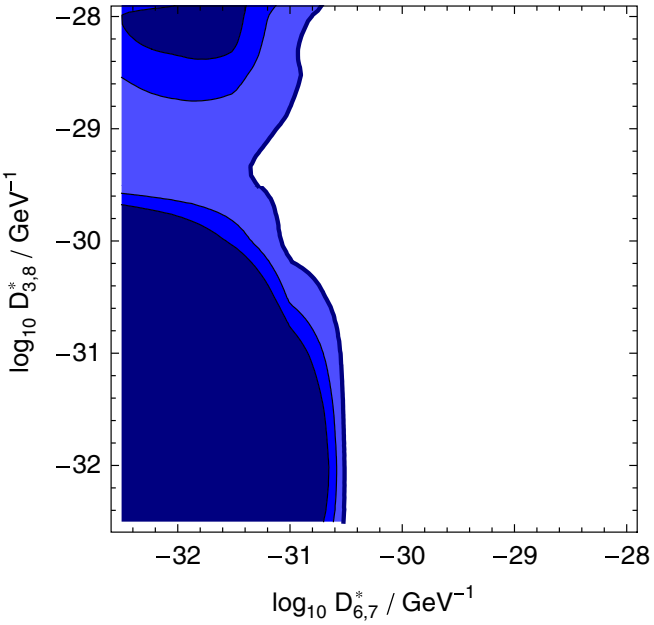


FIG. 8 (color online). 90%, 95%, and 99% CL allowed regions (from darkest to lightest) for QD effects with $n = 2$.

C. Determination of atmospheric flux

In the absence of evidence for violation of Lorentz invariance or quantum decoherence, we interpret the atmospheric neutrino flux in the context of standard model physics only. We use the likelihood analysis to perform a two-parameter forward-folding of the atmospheric neutrino flux to determine the normalization and any change in spectral index relative to existing models. As described in Sec. IV D, we test hypotheses of the form

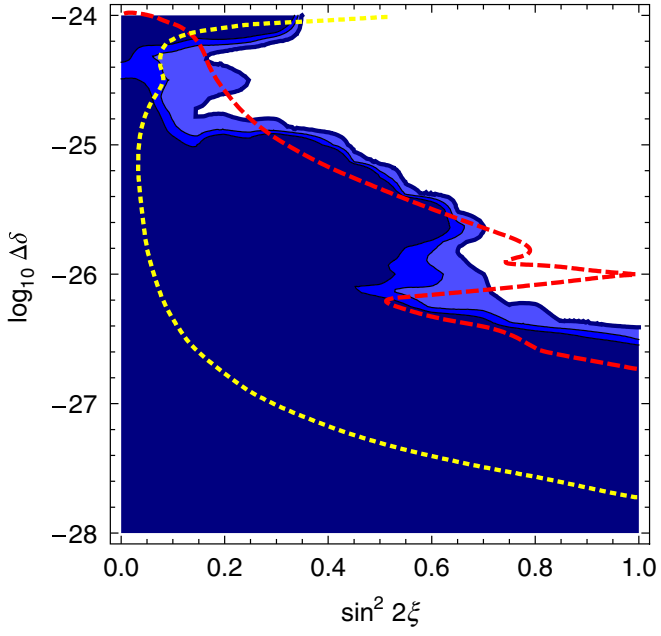


FIG. 7 (color online). 90%, 95%, and 99% CL allowed regions (from darkest to lightest) for VLI-induced oscillation effects with $n = 1$. Note we plot $\sin^2 2\xi$ to enhance the region of interest. Also shown are the Super-Kamiokande + K2K 90% contour [19] (dashed line), and the projected IceCube 10-year 90% sensitivity [70] (dotted line).

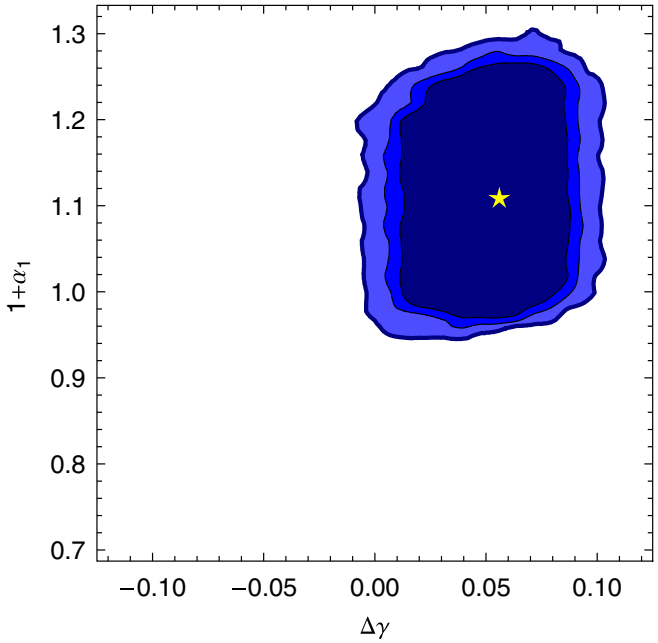


FIG. 9 (color online). 90%, 95%, and 99% allowed regions (from darkest to lightest) for the normalization $(1 + \alpha_1)$ and change in spectral index $(\Delta\gamma)$ of the conventional atmospheric neutrino flux, relative to Barr *et al.* [41]. The star marks the central best-fit point.

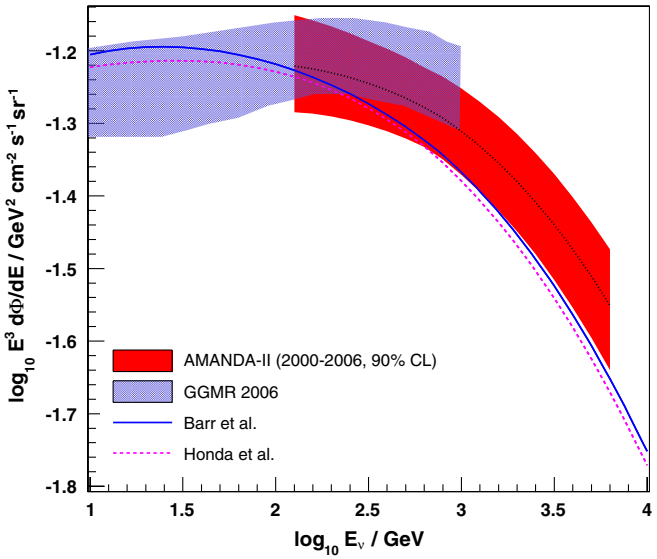


FIG. 10 (color online). Angle-averaged $\nu_\mu + \bar{\nu}_\mu$ atmospheric neutrino flux (solid band, 90% CL from the forward-folding analysis), multiplied by E^3 to enhance features. The dotted line shows the central best-fit curve. Also shown is a previous result by González-García *et al.* using Super-Kamiokande data [67], as well as Barr *et al.* [41] and Honda *et al.* [11] predictions. All fluxes are shown prior to oscillations.

$$\frac{d\Phi}{dE} = (1 + \alpha_1)\frac{d\Phi_{\text{ref}}}{dE}\left(\frac{E}{E_{\text{median}}}\right)^{\Delta\gamma}, \tag{13}$$

where $d\Phi_{\text{ref}}/dE$ is the differential Barr *et al.* or Honda *et al.* flux.

The allowed regions in the $\alpha_1 - \Delta\gamma$ parameter space are shown in Fig. 9. We display the band of allowed energy spectra in Fig. 10, where we have constructed the allowed region by forming the envelope of the set of curves allowed on the 90% contour in Fig. 9. The energy range of the band is the intersection of the 5%–95% regions of the allowed set of spectra, so restricted in order to limit the range of our constraints to an energy region in which AMANDA-II is sensitive.

The central best-fit point is also shown in Figs. 9 and 10. In fact, there is actually a range of best-fit points for the normalization, because of the degeneracy between the normalization parameter α_1 and the systematic error α_2. Specifically, we find the best-fit spectra to be

$$\frac{d\Phi_{\text{best-fit}}}{dE} = (1.1 \pm 0.1)\left(\frac{E}{640\ \text{GeV}}\right)^{0.056} \cdot \frac{d\Phi_{\text{Barr}}}{dE}, \tag{14}$$

for the energy range 120 GeV to 7.8 TeV, where the ± 0.1 is not the error on the fit but the range of possible best-fit values. This result is compatible with an analysis of Super-Kamiokande data [67] as well as an unfolding of the Fréjus data [68], and extends the Super-Kamiokande measurement by nearly an order of magnitude in energy. Our data suggest an atmospheric neutrino spectrum with a slightly harder spectral slope and higher normalization than either the Barr *et al.* or Honda *et al.* model. The likelihood ratio $\Delta\mathcal{L}$ of the unmodified Barr *et al.* spectrum [at the point (0,1) in Fig. 9] to the best-fit point is 4.9, corresponding to the 98% CL.

D. Discussion and future prospects

To summarize, we have set stringent upper limits on both Lorentz violation and quantum decoherence effects in the neutrino sector, with a VLI upper limit at the 90% CL of $\Delta\delta = \Delta c/c < 2.8 \times 10^{-27}$ for VLI oscillations proportional to the neutrino energy E, and a QD upper limit at the 90% CL of $D^* < 1.3 \times 10^{-31}$ GeV^{-1} for decoherence effects proportional to E^2. We have also set upper limits on VLI and QD effects with different energy dependencies. Finally, we have determined the atmospheric neutrino spectrum in the energy range from 120 GeV to 7.8 TeV and find a best-fit result that is slightly higher in normalization and has a harder spectral slope than either the Barr *et al.* or Honda *et al.* model. This result is consistent with Super-Kamiokande data and extends that measurement by nearly an order of magnitude in energy.

For an interpretation of the VLI and QD upper limits, we consider natural expectations for the values of such parameters. Given effects proportional to E^2 and E^3, one can argue via dimensional analysis that the new physics parameter should contain a power of the Planck mass M_{Pl} or M_{Pl}^2, respectively [69]. For example, for the decoherence parameters D, we may expect

$$D = D^* E_\nu^n = d^* \frac{E_\nu^n}{M_{\text{Pl}}^{n-1}}, \tag{15}$$

for $n \geq 2$, and d^* is a dimensionless quantity that is $O(1)$ by naturalness. From the limits in Table III we find $d^* < 1.6 \times 10^{-12}$ ($n = 2$) and $d^* < 910$ ($n = 3$). For the $n = 2$ case, the decoherence parameter is far below the natural expectation, suggesting either a stronger suppression than described, or that we have indeed probed beyond the Planck scale and found no decoherence of this type.

While the AMANDA-II data acquisition system used in this analysis ceased taking data at the end of 2006, the next-generation, cubic-kilometer-scale IceCube detector has the potential to improve greatly upon the limits presented here, as increased statistics of atmospheric neutrinos at the highest energies probe smaller deviations from the standard model. In particular, IceCube should be sensitive to $n = 1$ VLI effects an order of magnitude smaller than the limits from this analysis [70] (see also Fig. 7). We also note that we have also only tested one particular manifestation of VLI in the neutrino sector. A search of the atmospheric neutrino data for an unexpected directional dependence (for example, in right ascension) could probe other VLI effects, such as a universal directional asymmetry (see e.g. [71]).

Moving beyond searches with atmospheric neutrinos, once high energy astrophysical neutrinos are detected,

analysis of the flavor ratio at Earth can probe VLI, QD, and *CPT* violation [69,72]. Another technique is to probe VLI via the potential time delays between photons and neutrinos from gamma-ray bursts (GRBs). Given the cosmological distances traversed, this delay could range from 1 μs to 1 yr, depending on the power of suppression by $M_{\rm Pl}$ [73]. Detection of high energy neutrinos from multiple GRBs at different redshifts would allow either confirmation of the delay hypothesis or allow limits below current levels by several orders of magnitude [74]. Such a search is complicated by the low expected flux levels from individual GRBs, as well as uncertainty of any intrinsic $\gamma - \nu$ delay due to production mechanisms in the source (for a further discussion, see Ref. [75]). Other probes of Planck-scale physics may be possible as well, but ultimately this will depend on the characteristics of the neutrino sources detected.

ACKNOWLEDGMENTS

We acknowledge the support of the following agencies: the U.S. National Science Foundation—Office of Polar Programs; the U.S. National Science Foundation—Physics Division; the University of Wisconsin Alumni Research Foundation; the U.S. Department of Energy and National Energy Research Scientific Computing Center; the Louisiana Optical Network Initiative (LONI) grid computing resources; the Swedish Research Council; the Swedish Polar Research Secretariat; the Knut and Alice Wallenberg Foundation, Sweden; the German Ministry for Education and Research (BMBF); the Deutsche Forschungsgemeinschaft (DFG), Germany; the Fund for Scientific Research (FNRS-FWO), Flanders Institute to encourage scientific and technological research in industry (IWT); the Belgian Federal Science Policy Office (Belspo); and the Netherlands Organisation for Scientific Research (NWO). M. Ribordy acknowledges the support of the SNF (Switzerland), and A. Kappes and A. Groß acknowledge the support of the EU Marie Curie OIF Program.

APPEDIX A: FORMALISM

We present for the interested reader more details of the phenomenological background to the atmospheric ν_μ survival probabilities for the VLI and QD hypotheses that we test in this work.

1. Violation of lorentz invariance

The standard model extension (SME) provides an effective field-theoretic approach to VLI [76]. The ''minimal'' SME adds all coordinate-independent renormalizable Lorentz- and *CPT*-violating terms to the standard model Lagrangian. Even when restricted to first order effects in the neutrino sector, the SME results in numerous potentially observable effects [71,77,78]. To specify one particular model that leads to alternative oscillations at high energy, we consider only the Lorentz-violating Lagrangian term

$$\tfrac{1}{2} i (c_L)_{\mu\nu ab} \bar{L}_a \gamma^\mu \overleftrightarrow{D}^\nu L_b, \tag{A1}$$

with the VLI parametrized by the dimensionless coefficient c_L [77]. L_a and L_b are left-handed neutrino doublets with indices running over the generations e, μ, and τ, and D^ν is the covariant derivative with $A\overleftrightarrow{D}^\nu B \equiv AD^\nu B - (D^\nu A)B$.

We restrict ourselves to rotationally invariant scenarios with only nonzero time components in c_L, and we consider only a two-flavor system. The eigenstates of the resulting 2×2 matrix c_L^{TT} correspond to differing maximal attainable velocity (MAV) eigenstates. These may be distinct from either the flavor or mass eigenstates. Any difference Δc in the eigenvalues will result in neutrino oscillations. The above construction is equivalent to a modified dispersion relationship of the form

$$E^2 = p^2 c_a^2 + m^2 c_a^4, \tag{A2}$$

where c_a is the MAV for a particular eigenstate, and in general $c_a \neq c$ [17,18]. Given that the mass is negligible, the energy difference between two MAV eigenstates is equal to the VLI parameter $\Delta c/c = (c_{a1} - c_{a2})/c$, where c is the canonical speed of light.

The effective Hamiltonian $H_\pm$ representing the energy shifts from both mass-induced and VLI oscillations can be written [19]

$$H_\pm = \frac{\Delta m^2}{4E} \mathbf{U}_\theta \begin{pmatrix} -1 & 0 \\ 0 & 1 \end{pmatrix} \mathbf{U}_\theta^\dagger + \frac{\Delta c}{c} \frac{E}{2} \mathbf{U}_\xi \begin{pmatrix} -1 & 0 \\ 0 & 1 \end{pmatrix} \mathbf{U}_\xi^\dagger, \tag{A3}$$

with two mixing angles θ and ξ. The associated 2×2 mixing matrices are

$$U_\theta = \begin{pmatrix} \cos\theta & \sin\theta \\ -\sin\theta & \cos\theta \end{pmatrix}, \tag{A4}$$

and

$$U_\xi = \begin{pmatrix} \cos\xi & \sin\xi e^{\pm i\eta} \\ -\sin\xi e^{\mp i\eta} & \cos\xi \end{pmatrix}, \tag{A5}$$

with η representing their relative phase. Solving the Louiville equation for time evolution of the state density matrix ρ,

$$\dot{\rho} = -i[H_\pm, \rho] \tag{A6}$$

results in the ν_μ survival probability in Eq. (2). We refer the reader to Ref. [19] for more detail.

2. Quantum decoherence

Several constructions exist of a phenomenological framework for quantum decoherence effects [79]. A common approach is to modify the time-evolution of the density matrix ρ with a dissipative term $\not{\partial} H \rho$:

$$\dot{\rho} = -i[H, \rho] + \not{\delta} H\rho. \tag{A7}$$

One method to model such an open system is via the technique of Lindblad quantum dynamical semigroups [80]. Here we outline the approach in Ref. [32], to which we refer the reader for more detail. In this case we have a set of self-adjoint environmental operators A_j, and Eq. (A7) becomes

$$\dot{\rho} = -i[H, \rho] + \frac{1}{2}\sum_j ([A_j, \rho A_j] + [A_j\rho, A_j]). \tag{A8}$$

The hermiticity of the A_j ensures the monotonic increase of entropy, and in general, pure states will now evolve to mixed states. The irreversibility of this process implies *CPT* violation [79].

To obtain specific predictions for the neutrino sector, there are again several approaches for both two-flavor systems [35,81] and three-flavor systems [32,82]. Again, we follow the approach in [32] for a three-flavor neutrino system including both decoherence and mass-induced oscillations. The dissipative term in Eq. (A8) is expanded in the Gell-Mann basis F_μ, $\mu \in \{0, \ldots, 8\}$, such that

$$\frac{1}{2}\sum_j ([A_j, \rho A_j] + [A_j\rho, A_j]) = \sum_{\mu,\nu} L_{\mu\nu}\rho_\mu F_\nu. \tag{A9}$$

At this stage we must choose a form for the decoherence matrix $L_{\mu\nu}$, and we select the weak-coupling limit in which L is diagonal, with $L_{00} = 0$ and $L_{ii} = -D_i$, $i \in \{1, \ldots, 8\}$. The D_i are in energy units, and their inverses represent the characteristic length scale(s) over which decoherence effects occur. Solving this system for atmospheric neutrinos (where we neglect mass-induced oscillations other than $\nu_\mu \rightarrow \nu_\tau$) results in the ν_μ survival probability given in Eq. (8).

In Eq. (8), we must impose the condition $\Delta m^2/E > |D_6 - D_7|$, but this is not an issue in the parameter space we explore in this analysis. If one wishes to ensure strong conditions such as complete positivity [81], there may be other inequalities that must be imposed (see e.g. the discussion in Ref. [82]).

[1] R. Gambini and J. Pullin, Phys. Rev. D **59**, 124021 (1999).
[2] J. Madore, S. Schraml, P. Schupp, and J. Wess, Eur. Phys. J. C **16**, 161 (2000).
[3] V. A. Kostelecký and S. Samuel, Phys. Rev. D **39**, 683 (1989).
[4] G. Amelino-Camelia, C. Lämmerzahl, A. Macias, and H. Müller, in *Gravitation and Cosmology*, edited by A. Macias *et al.*, AIP Conf. Proc. No. 758 (AIP, New York, 2005).
[5] D. Mattingly, Living Rev. Relativity **8**, 5 (2005).
[6] S. W. Hawking, Commun. Math. Phys. **87**, 395 (1982).
[7] V. A. Balkanov *et al.*, Astropart. Phys. **12**, 75 (1999).
[8] E. Andrés *et al.*, Nature (London) **410**, 441 (2001).
[9] J. A. Aguilar *et al.*, Astropart. Phys. **26**, 314 (2006).
[10] J. Ahrens *et al.*, Astropart. Phys. **20**, 507 (2004).
[11] M. Honda, T. Kajita, K. Kasahara, S. Midorikawa, and T. Sanuki, Phys. Rev. D **75**, 043006 (2007).
[12] G. D. Barr, S. Robbins, T. K. Gaisser, and T. Stanev, Phys. Rev. D **74**, 094009 (2006).
[13] Y. Ashie *et al.*, Phys. Rev. Lett. **93**, 101801 (2004).
[14] M. Sanchez *et al.*, Phys. Rev. D **68**, 113004 (2003).
[15] M. Ambrisio *et al.*, Phys. Lett. B **566**, 35 (2003).
[16] G. L. Fogli *et al.*, Phys. Rev. D **78**, 033010 (2008).
[17] S. Coleman and S. L. Glashow, Phys. Rev. D **59**, 116008 (1999).
[18] S. L. Glashow, arXiv:hep-ph/0407087.
[19] M. C. González-García and M. Maltoni, Phys. Rev. D **70**, 033010 (2004).
[20] M. Maltoni, T. Schwetz, M. Tórtola, and J. W. F. Valle, New J. Phys. **6**, 122 (2004).
[21] G. Battistoni *et al.*, Phys. Lett. B **615**, 14 (2005).
[22] G. L. Fogli, E. Lisi, A. Marrone, and G. Scioscia, Phys. Rev. D **60**, 053006 (1999).
[23] M. H. Ahn *et al.*, Phys. Rev. Lett. **90**, 041801 (2003).
[24] J. Ahrens and J. L. Kelley *et al.*, in *Proceedings of 30th ICRC, Mérida, Mexico, 2007* edited by R. Caballero *et al.* (Universidad Nacional Autónoma de México, Mexico City, 2007).
[25] D. Morgan, E. Winstanley, J. Brunner, and L. F. Thompson, Astropart. Phys. **29**, 345 (2008).
[26] J. Alfaro, H. A. Morales-Técotl, and L. F. Urrutia, Phys. Rev. Lett. **84**, 2318 (2000).
[27] R. Brustein, D. Eichler, and S. Foffa, Phys. Rev. D **65**, 105006 (2002).
[28] M. Gasperini, Phys. Rev. D **38**, 2635 (1988).
[29] A. Halprin and C. N. Leung, Phys. Rev. Lett. **67**, 1833 (1991).
[30] G. Z. Adunas, E. Rodriquez-Milla, and D. V. Ahluwalia, Phys. Lett. B **485**, 215 (2000).
[31] J. Ellis, J. S. Hagelin, D. V. Nanopoulos, and M. Srednicki, Nucl. Phys. B **241**, 381 (1984).
[32] A. M. Gago, E. M. Santos, W. J. C. Teves, and R. Zukanovich Funchal, arXiv:hep-ph/0208166.
[33] J. Ellis, N. E. Mavromatos, and D. V. Nanopoulos, Mod. Phys. Lett. A **12**, 1759 (1997); J. Ellis, N. E. Mavromatos, D. V. Nanopoulos, and E. Winstanley, Mod. Phys. Lett. A **12**, 243 (1997).
[34] E. Lisi, A. Marrone, and D. Montanino, Phys. Rev. Lett. **85**, 1166 (2000).
[35] D. Morgan, E. Winstanley, J. Brunner, and L. Thompson, Astropart. Phys. **25**, 311 (2006).
[36] G. L. Fogli, E. Lisi, A. Marrone, and D. Montanino, Phys. Rev. D **67**, 093006 (2003).

[37] G. L. Fogli, E. Lisi, A. Marrone, D. Montanino, and A. Palazzo, Phys. Rev. D **76**, 033006 (2007).
[38] M. Ackermann *et al.*, J. Geophys. Res. **111**, D13203 (2006).
[39] J. Ahrens *et al.*, Nucl. Instrum. Methods Phys. Res., Sect. A **524**, 169 (2004).
[40] G. C. Hill, Astropart. Phys. **6**, 215 (1997).
[41] G. D. Barr, T. K. Gaisser, P. Lipari, S. Robbins, and T. Stanev, Phys. Rev. D **70**, 023006 (2004).
[42] T. K. Gaisser, *Cosmic Rays and Particle Physics* (Cambridge University Press, Cambridge, 1991), p. 88.
[43] D. Chirkin and W. Rhode, arXiv:hep-ph/0407075.
[44] J. Lundberg *et al.*, Nucl. Instrum. Methods Phys. Res., Sect. A **581**, 619 (2007).
[45] S. Hundertmark, Report No. DESY-PROC-1999-01, 1999; S. Hundertmark, Ph.D. thesis, Humboldt Universität zu Berlin, 1999.
[46] D. Heck *et al.*, Forschungszentrum Karlsruhe Report No. FZKA 6019, 1998.
[47] A. Achterberg *et al.*, Phys. Rev. D **75**, 102001 (2007).
[48] T. Neunhöffer, Astropart. Phys. **25**, 220 (2006).
[49] T. DeYoung *et al.*, in *Proceedings of the Conference on Advanced Statistical Techniques in Particle Physics, Durham, UK, 2000*, edited by M. R. Whalley and L. Lyons (Inst. for Part. Phys. Phenom., Durham, 2002) p. 235.
[50] R. Abbasi *et al.*, Phys. Rev. D **79**, 062001 (2009).
[51] G. J. Feldman and R. D. Cousins, Phys. Rev. D **57**, 3873 (1998).
[52] R. Cousins, in *Statistical Problems in Particle Physics, Astrophysics and Cosmology: Proceedings of PHYSTAT05, Oxford, UK, 2005*, edited by L. Lyons and M. Ünel (Imperial College Press, London, 2005).
[53] A. Stuart, K. Ord, and S. Arnold, *Kendall's Advanced Theory of Statistics* (Arnold, London, 1999), 6th ed., Vol. 2A.
[54] F. James and M. Roos, Comput. Phys. Commun. **10**, 343 (1975).
[55] W. A. Rolke and A. M. López, Nucl. Instrum. Methods Phys. Res., Sect. A **458**, 745 (2001).
[56] W. A. Rolke, A. M. López, and J. Conrad, Nucl. Instrum. Methods **A551**, 493 (2005).
[57] G. J. Feldman, "Multiple Measurements and Parameters in the Unified Approach," in Workshop on Confidence Limits, Chicago, Fermilab, 2000 (unpublished), http://conferences.fnal.gov/cl2k.
[58] K. Cranmer, in *Statistical Problems in Particle Physics, Astrophysics and Cosmology: Proceedings of PHYSTAT05, Oxford, UK, 2005*, edited by L. Lyons and M. Ünel (Imperial College Press, London, 2005).
[59] M. Kowalski and A. Gazizov, Comput. Phys. Commun. **172**, 203 (2005).
[60] H. L. Lai *et al.*, Eur. Phys. J. C **12**, 375 (2000).
[61] A. D. Martin, R. G. Roberts, and W. J. Stirling, Phys. Lett. B **354**, 155 (1995).
[62] R. S. Fletcher, T. K. Gaisser, P. Lipari, and T. Stanev, Phys. Rev. D **50**, 5710 (1994); R. Engel, T. K. Gaisser, P. Lipari, and T. Stanev, in *Proceedings of 26th ICRC, Salt Lake City, Utah, 1999* edited by D. Kieda, M. Salamon, and B. Dingus (University of Utah, Salt Lake City, 1999), p. 415.
[63] K. Werner, F.-M. Liu, and T. Pierog, Phys. Rev. C **74**, 044902 (2006).
[64] S. Ostapchenko, Phys. Lett. B **636**, 40 (2006); S. Ostapchenko, Phys. Rev. D **74**, 014026 (2006).
[65] G. Fiorentini, A. Naumov, and F. L. Villante, Phys. Lett. B **510**, 173 (2001); E. V. Bugaev *et al.*, Nuovo Cimento Soc. Ital. Fis. **12C**, 41 (1989).
[66] S. Mizobuchi *et al.*, in *Proceedings of 29th ICRC, Pune, India, 2005* (Tata Institute of Fundamental Research, Mumbai, 2005), p. 323; A. Djannati-Ataï *et al.*, Astron. Astrophys. **350**, 17 (1999).
[67] M. C. González-García, M. Maltoni, and J. Rojo, J. High Energy Phys. 10 (2006) 075.
[68] K. Daum, W. Rhode, P. Bareyre, and R. Barloutaud, Z. Phys. C **66**, 417 (1995).
[69] L. A. Anchordoqui *et al.*, Phys. Rev. D **72**, 065019 (2005).
[70] M. C. González-García, F. Halzen, and M. Maltoni, Phys. Rev. D **71**, 093010 (2005).
[71] V. A. Kostelecký and M. Mewes, Phys. Rev. D **69**, 016005 (2004).
[72] D. Hooper, D. Morgan, and E. Winstanley, Phys. Rev. D **72**, 065009 (2005).
[73] G. Amelino-Camelia, Int. J. Mod. Phys. D **12**, 1633 (2003).
[74] U. Jacob and T. Piran, Nature Phys. **3**, 87 (2007).
[75] M. C. González-García and F. Halzen, J. Cosmol. Astropart. Phys. 2 (2007) 008.
[76] D. Colladay and V. A. Kostelecký, Phys. Rev. D **58**, 116002 (1998).
[77] V. A. Kostelecký and M. Mewes, Phys. Rev. D **70**, 031902 (R) (2004).
[78] T. Katori, V. A. Kostelecký, and R. Tayloe, Phys. Rev. D **74**, 105009 (2006).
[79] N. E. Mavromatos, Lect. Notes Phys. **669**, 245 (2005).
[80] G. Lindblad, Commun. Math. Phys. **48**, 119 (1976).
[81] F. Benatti and R. Floreanini, J. High Energy Phys. 02 (2000) 032.
[82] G. Barenboim, N. E. Mavromatos, S. Sarkar, and A. Waldron-Lauda, Nucl. Phys. **B758**, 90 (2006).